Band Structure and Fermi Surface for Rhenium

L. F. MATTHEISS

Bell Telephone Laboratories, Murray Hill, New Jersey

(Received 7 June 1966)

Band-structure calculations for hexagonal close-packed rhenium have been performed using the relativistic augmented-plane-wave (APW) method. From these energy-band results, a theoretical model for the rhenium Fermi surface has been determined. This Fermi surface is found to consist of five sheets, including closed-hole sections in the fifth, sixth, and seventh zones, an open eighth-zone electron sheet, and a closed ninth-zone electron piece. The detailed size, shape, and general topology of this Fermi surface appear to be in reasonable quantitative agreement with de Haas–van Alphen, magnetoacoustic, and magnetoresistance data. Spin-orbit coupling is found to play an essential role in determining the Fermi-surface topology in rhenium, since it is responsible for changing the connectivity of several sheets of the Fermi surface. The density of states exhibits some interesting structure, most of which lies below the rhenium Fermi level. Assuming a rigid-band model for the density of states, the specific-heat data for hexagonal W-Re and Re-Os disordered alloys are found to be in good agreement with the calculated density-of-states when the experimental results are corrected for phonon-enhancement effects, as calculated by McMillan.

I. INTRODUCTION

THE simplest approach to the theory of electrons in metals involves the one-electron or independent-particle model. It is now generally believed that this model is valid for transition as well as simple metals. Now that detailed experimental Fermi-surface information is becoming available for transition metals, it is important to determine whether or not these experimental results are consistent with the predictions of this model. Of all the transition metals, the experimental Fermi-surface data for bcc tungsten appears to be the most complete at the present time. In this case, it has been possible to obtain quantitative agreement between band theory and experiment regarding the size, shape, and topology of the tungsten Fermi surface.[1,2] Extensive experimental Fermi-surface information is also becoming available for hexagonal close-packed rhenium, which is situated next to tungsten in the Periodic Table. The purpose of the present paper is twofold: (1) to present a theoretical model for the rhenium Fermi surface that has been derived from relativistic band-structure calculations; and (2) to compare this theoretical Fermi surface with the available experimental results.

The most precise experimental information about the rhenium Fermi surface has been provided by Joseph and Thorsen[3] from an analysis of their low-field de Haas-van Alphen (dHvA) data. They find that two small closed Fermi-surface segments, located along the AL symmetry line of the hexagonal Brillouin zone, can account for most of their data. These segments consist of an ellipsoid nested within a dumbbell-shaped piece, such that the two sheets contact along the AL line, thereby leading to magnetic-breakdown phenomena. The magnetoacoustic data of Jones and Rayne[4] yield

caliper dimensions for some of the smaller as well as the larger sections of the rhenium Fermi surface. These results are supplemented by the more extensive magnetoacoustic data of Testardi,[5] which yield caliper dimensions which range in size from those of the ellipsoid and dumbbell to dimensions which are several times larger. The extremal areas of these larger pieces have been observed also in the pulsed-field dHvA data of Thorsen and Joseph.[6] Finally, the high-field magnetoresistance measurements by Reed, Fawcett, and Soden[7] indicate that the rhenium Fermi surface supports open orbits along the [0001] and $\langle 10\bar{1}0 \rangle$ directions, the latter resulting from magnetic breakdown. In addition, they find two-dimensional regions of aperiodic open orbits when the magnetic field is near the $\langle 11\bar{2}0 \rangle$ axes.

In order to provide a theoretical model for the rhenium Fermi surface, the rhenium band structure has been calculated using the augmented-plane-wave (APW) method. Although the initial calculations were nonrelativistic, it soon became apparent from the nature of the results that relativistic effects (especially spin-orbit coupling) would play an important role in determining the Fermi-surface topology. Consequently, the calculations were repeated using a relativistic variation of the APW method that has been proposed by Loucks.[8]

It is possible to rewrite Loucks' expressions for the relativistic APW matrix elements so that the relationship between the relativistic and nonrelativistic APW methods is more transparent. These results are included in the following section. Section III contains the details of the calculation, including a discussion of the potential, lattice constants, and computational techniques. The results of the calculation are presented in Sec. IV, including the energy bands, a density of states, and the Fermi surface for rhenium. These results are compared

[1] L. F. Mattheiss, Phys. Rev. **139**, A1893 (1965).
[2] T. L. Loucks, Phys. Rev. Letters **14**, 693 (1965); Phys. Rev. **139**, A1181 (1965); **143**, 506 (1966).
[3] A. S. Joseph and A. C. Thorsen, Phys. Rev. **133**, A1546 (1964).
[4] C. K. Jones and J. A. Rayne, Phys. Rev. **139**, A1876 (1965).

[5] L. R. Testardi (to be published).
[6] A. C. Thorsen, A. S. Joseph, and L. E. Valby, Phys. Rev. (to be published).
[7] W. A. Reed, E. Fawcett, and R. R. Soden, Phys. Rev. **139**, A1557 (1965).
[8] T. L. Loucks, Phys. Rev. **139**, A1333 (1965).

with experiment in Sec. V. The final section contains a discussion of the results.

II. METHOD OF CALCULATION

Using a variational procedure, Loucks has derived a relativistic variation of the APW method which is useful for calculating the band structures of heavier elements and compounds.[8] Loucks' work represents a natural extension of the nonrelativistic APW method that was proposed by Slater in 1937.[9] In both cases, the crystal potential is approximated by a "muffin-tin" potential. This "muffin-tin" potential consists of spheres surrounding each atomic site within which the potential is assumed to be spherically symmetric and regions between the spheres where the potential is assumed to be constant. The solution to the Schrödinger equation (or its relativistic equivalent) is represented by a linear combination of APW basis functions, the coefficients and eigenvalues being determined from the appropriate secular equations. In both the relativistic and nonrelativistic methods, these basis functions are composite in nature, consisting of central-field expansions inside the spheres and a plane wave in the region between the spheres. In the relativistic APW method, the solutions inside the spheres are expanded in terms of four-component central-field orbitals of the Dirac Hamiltonian. In the region between the spheres, the wave function is a Dirac plane wave. The coefficients for the upper two components of the central-field orbitals are determined by the condition that they match the upper two components of the Dirac plane wave at the sphere radii.

Using Green's theorem, an expression equivalent to that derived by Loucks for the relativistic APW matrix elements has been obtained. In this revised form, the relativistic APW matrix element between basis functions with wave vectors $\mathbf{k}_i$, $\mathbf{k}_j$ and spins μ, ν is given by

$$(H-E)_{ij}^{\mu\nu} = (\mathbf{k}_i \cdot \mathbf{k}_j - E)\delta_{\mu\nu}\delta_{ij}$$
$$+ \Omega^{-1} \sum_n e^{i(\mathbf{k}_j - \mathbf{k}_i) \cdot \mathbf{r}_n} F_{n,ij}^{\mu\nu}, \quad (1)$$

where

$$F_{n,ij}^{\mu\nu} = 4\pi R_n^2 \left\{ -(\mathbf{k}_i \cdot \mathbf{k}_j - E)\frac{j_1(|\mathbf{k}_j - \mathbf{k}_i|R_n)}{|\mathbf{k}_j - \mathbf{k}_i|}\delta_{\mu\nu} \right.$$
$$\left. + \sum_\kappa D_{\kappa,ij}^{\mu\nu} j_l(|\mathbf{k}_i|R_n) j_l(|\mathbf{k}_j|R_n)\eta_\kappa(R_n,E) \right\}, \quad (2)$$

and

$$\eta_\kappa(R_n,E) = cf_\kappa(R_n,E)/g_\kappa(R_n,E) - [(\kappa+1)/R_n]. \quad (3)$$

In Eqs. (1)–(3), which are written in atomic units, $\mathbf{r}_n$ is a vector from an arbitrary origin to the nth atom in the unit cell, whose sphere radius is R_n. The unit cell volume is Ω, and $j_l(x)$ are spherical Bessel functions. The quanti-

[9] J. C. Slater, Phys. Rev. **51**, 846 (1937).

ties $D_{\kappa,ij}^{\mu\nu}$ and $cf_\kappa(R_n,E)/g_\kappa(R_n,E)$ have been defined by Loucks.[8] The latter quantity represents the velocity of light times the ratio of the large to the small components of the Dirac central-field orbitals, evaluated at the sphere radius R_n for energy E. The indices on $(H-E)$ and D_κ have been transposed in Eqs. (1) and (2) so that $(H-E)_{ij}^{\mu\nu}$ and $D_{\kappa,ij}^{\mu\nu}$ are equivalent to

$$M\binom{j\nu}{i\mu} \quad \text{and} \quad D_\kappa\binom{j\nu}{i\mu}$$

in Loucks' notation. Also, the present equations describe the general situation where the crystal structure contains an arbitrary number of atoms per unit cell at vector positions $\mathbf{r}_n$.

For purposes of comparison, it is useful to write down the corresponding expressions for the nonrelativistic APW method[9]:

$$(H-E)_{ij} = (\mathbf{k}_i \cdot \mathbf{k}_j - E)\delta_{ij} + \Omega^{-1} \sum_n e^{i(\mathbf{k}_j - \mathbf{k}_i) \cdot \mathbf{r}_n} F_{n,ij}, \quad (4)$$

where

$$F_{n,ij} = 4\pi R_n^2 \left\{ -(\mathbf{k}_i \cdot \mathbf{k}_j - E)\frac{j_1(|\mathbf{k}_j - \mathbf{k}_i|R_n)}{|\mathbf{k}_j - \mathbf{k}_i|} \right.$$
$$+ \sum_{l=0}^{\infty}(2l+1)P_l(\hat{k}_i \cdot \hat{k}_j) j_l(|\mathbf{k}_i|R_n) j_l(|\mathbf{k}_j|R_n)$$
$$\left. \times u_{nl}'(R_n,E)/u_{nl}(R_n,E) \right\}. \quad (5)$$

In Eq. (5), $\hat{k}_i$ signifies a unit vector and the quantities $u_{nl}'(R_n,E)/u_{nl}(R_n,E)$ represent the logarithmic derivatives of the (nl) solution to the radial Schrödinger equation for energy E, again evaluated at the sphere radius R_n. The relationship between the relativistic and nonrelativistic APW methods becomes more transparent when the detailed expressions for $F_{n,ij}^{++}$ and $F_{n,ij}^{+-}$ are examined:

$$F_{n,ij}^{+-} = 4\pi R_n^2 \left\{ -(\mathbf{k}_i \cdot \mathbf{k}_j - E)\frac{j_1(|\mathbf{k}_j - \mathbf{k}_i|R_n)}{|\mathbf{k}_j - \mathbf{k}_i|} \right.$$
$$+ \sum_{l=0}^{\infty} P_l(\hat{k}_i \cdot \hat{k}_j) j_l(|\mathbf{k}_i|R_n) j_l(|\mathbf{k}_j|R_n)$$
$$\times [l\eta_l^-(R_n,E) + (l+1)\eta_l^+(R_n,E)]$$
$$+ i(\hat{k}_j \times \hat{k}_i)_z \sum_{l=0}^{\infty} P_l'(\hat{k}_i \cdot \hat{k}_j) j_l(|\mathbf{k}_i|R_n)$$
$$\left. \times j_l(|\mathbf{k}_j|R_n)[\eta_l^+(R_n,E) - \eta_l^-(R_n,E)] \right\}; \quad (6)$$

$$F_{n,ij}^{+-} = 4\pi R_n^2 \{(\hat{k}_j \times \hat{k}_i)_y + i(\hat{k}_j \times \hat{k}_i)_x\}$$
$$\times \{\sum_{l=0}^{\infty} P_l'(\hat{k}_i \cdot \hat{k}_j) j_l(|\mathbf{k}_i|R_n) j_l(|\mathbf{k}_j|R_n)$$
$$\times [\eta_l^+(R_n,E) - \eta_l^-(R_n,E)]\}. \quad (7)$$

FIG. 1. The Brillouin zone for the hexagonal structure with symmetry points and lines labeled according to the standard notation.

In Eqs. (6) and (7), $\eta_i^{\pm}(R_n,E)$ correspond to states with $j=l\pm\frac{1}{2}$, and the primes indicate differentiation with respect to the argument. As Loucks has pointed out,

$$\lim_{c\to\infty}\left[\frac{cf_\kappa(R_n,E)}{g_\kappa(R_n,E)}-\left(\frac{\kappa+1}{R_n}\right)\right]=\frac{u_{nl}'(R_n,E)}{u_{nl}(R_n,E)}. \qquad (8)$$

Therefore, in the nonrelativistic limit,

$$\eta_i^+(R_n,E)=\eta_i^-(R_n,E)=u_{nl}'(R_n,E)/u_{nl}(R_n,E),$$
$$F_{n,ij}^{++}=F_{n,ij}, \qquad (9)$$
$$F_{n,ij}^{+-}=0.$$

The above expressions for $F_{n,ij}^{++}$ and $F_{n,ij}^{+-}$ have been used in the present calculations.

These expressions for $F_{n,ij}^{++}$ and $F_{n,ij}^{+-}$ are useful from another point of view. Namely, in these equations, the various relativistic effects are distinguished clearly. The Darwin and mass-velocity effects are included in the relativistic equivalent to $(2l+1)u_{nl}'(R_n,E)/u_{nl}(R_n,E)$, which is $[l\eta_i^-(R_n,E)+(l+1)\eta_i^+(R_n,E)]$. As a result, it is possible to include the Darwin and mass-velocity corrections in a nonrelativistic calculation simply by replacing $(2l+1)u_{nl}'(R_n,E)/u_{nl}(R_n,E)$ with $[l\eta_i^-(R_n,E)+(l+1)\eta_i^+(R_n,E)]$, provided one is willing to neglect the spin-orbit terms. Since the Darwin and mass-velocity corrections are expected in many cases to be much larger than the spin-orbit corrections,[10] this allows one to obtain rather simply a good first approximation to the relativistic band structure of a metal or compound. When necessary, spin-orbit effects can be estimated by means of perturbation theory.

Expressions similar to Eqs. (6) and (7) have been derived previously by Dimmock,[11] who introduced relativistic effects using the Pauli rather than the Dirac theory. As a matter of fact, the derivation of Eqs. (6)

and (7) was motivated by a desire to understand the relationship between these two approaches.

III. DETAILS OF THE CALCULATION

For the hexagonal close-packed structure, energy-band calculations are simplified when the origin of the unit cell is chosen to be at the center of inversion rather than at an atomic site. With this choice, the structure factors are real and Eq. (1) can be written

$$(H-E)_{ij}{}^{\mu\nu}=(\mathbf{k}_i\cdot\mathbf{k}_j-E)\delta_{\mu\nu}\delta_{ij}$$
$$+2\Omega^{-1}\cos(\mathbf{k}_j-\mathbf{k}_i)\cdot\mathbf{r}_n F_{ij}{}^{\mu\nu}. \quad (10)$$

Here, $\mathbf{r}_n$ is a vector from the inversion center to one of the six pairs of neighboring atoms. The index n has been dropped from $F_{ij}{}^{\mu\nu}$ in Eq. (10) since the atoms within the spheres at $\pm\mathbf{r}_n$ are identical in the hexagonal close-packed structure. If the primitive lattice vectors are written

$$\mathbf{t}_1=(a/2)(\sqrt{3}\mathbf{i}+\mathbf{j}), \quad \mathbf{t}_2=a\mathbf{j}, \quad \mathbf{t}_3=c\mathbf{k}, \quad (11)$$

then one choice for $\mathbf{r}_n$ is given by

$$\mathbf{r}_n=\tfrac{1}{3}\mathbf{t}_1+\tfrac{2}{3}\mathbf{t}_2+\tfrac{1}{4}\mathbf{t}_3. \qquad (12)$$

Using the primitive lattice vectors of Eq. (11), the wave vectors $\mathbf{K}_n$ have the form $\mathbf{K}_n=n_1\mathbf{b}_1+n_2\mathbf{b}_2+n_3\mathbf{b}_3$, where the n_i are integers and

$$\mathbf{b}_1=(4\pi/\sqrt{3}a)\mathbf{i}; \quad \mathbf{b}_2=(2\pi/\sqrt{3}a)(\mathbf{i}+\sqrt{3}\mathbf{j}); \qquad (13)$$
$$\mathbf{b}_3=(2\pi/c)\mathbf{k}.$$

The Brillouin zone for the hexagonal structure is shown in Fig. 1. The various symmetry points and lines in 1/24 the Brillouin zone are labeled in accordance with the notation of Herring.[12]

Using the room-temperature lattice constants and the linear expansion coefficients for rhenium that are tabulated in Pearson,[13] the lattice constants at 4.2°K have been estimated. The following values have been used in the present calculations:

$$a=2.758\text{ Å}=5.211\text{ atomic units(a.u.)}$$
$$c=4.447\text{ Å}=8.404\text{ a.u.}$$

Since the c/a ratio (1.613) is less than the ideal close-packed ratio (1.633), the maximum sphere radius R_n is 2.584 a.u. rather than $a/2$.

Essentially, two separate relativistic energy-band calculations have been carried through for rhenium. In the first calculation, spin-orbit coupling has been omitted, though the Darwin and mass-velocity corrections have been included by replacing

$$(2l+1)u_{nl}'(R_n,E)/u_{nl}(R_n,E)$$
with
$$[l\eta_i^-(R_n,E)+(l+1)\eta_i^+(R_n,E)],$$

[10] F. Herman, C. D. Kuglin, K. F. Cuff, and R. L. Kortum, Phys. Rev. Letters 11, 541 (1963).
[11] J. O. Dimmock (private communication).

[12] C. Herring, J. Franklin Inst. 233, 525 (1942).
[13] W. B. Pearson, A Handbook of Lattice Spacings and Structures of Metals and Alloys (Pergamon Press, Inc., New York, 1958).

as discussed in the previous section. In this approxima-
tion, the symmetry of the energy-band states can be
represented in terms of the single-group notation of
Herring.[12] The symmetrized version of the APW pro-
gram that has been used in this calculation is similar to
that described by Wood for the fcc and bcc cubic
structures.[14] The fact that the space group for the
hexagonal close-packed structure is nonsymmorphic
introduces only minor complications. By choosing the
origin of coordinates at the center of inversion, the APW
matrix can be made real at all points in the Brillouin
zone. However, for states with reduced wave vectors
lying in the ALH plane, it was necessary generally to
utilize only a subgroup of the wave-vector group to ob-
tain a real matrix.

When spin-orbit coupling is included in the calcula-
tions, it is clear from Eqs. (6) and (7) that the APW
matrix is inherently complex. Furthermore, the size of
the matrix is doubled for a given set of nonrelativistic
APW basis functions. For convenience, the fully rela-
tivistic calculations have been carried out using un-
symmetrized basis functions. Consequently, it has not
been possible to label the symmetry properties of the
individual states. Such a limitation would be rather
serious in a nonrelativistic calculation, where the energy
bands with different symmetries frequently cross along
symmetry lines and in symmetry planes, leading to
accidental degeneracies. However, as Elliott has shown,
the double group for the hexagonal close-packed struc-
ture contains relatively few "extra" representations
along symmetry directions.[15] This result reduces the
possibility of accidental degeneracies caused by crossing
bands in symmetry directions and determines the con-
nectivity of the bands in most cases. According to
Elliott, there is only one "extra" representation in the
Σ, T, T', and R directions of the Brillouin zone, so that
band crossings are forbidden in these directions. Acci-
dental degeneracies caused by crossing bands are possi-
ble in the Δ, P, S, and S' directions, however.

A similar simplification occurs in the symmetry
planes of the hexagonal close-packed Brillouin zone
when spin-orbit coupling is introduced. Falicov and
Cohen have analyzed the situation in the ALH plane.[16]
According to their results, band crossing are possible
anywhere in the ALH plane, except along the R direc-
tion. A similar analysis for the other symmetry planes
of the Brillouin zone shows that band crossings do not
occur. Spin-orbit coupling removes the accidental
degeneracies which exist between the nonrelativistic
states that are even and odd under reflection in these
symmetry planes.

The increased size and complex nature of the rela-
tivistic APW matrix require efficient computer pro-
grams, even on a high-speed computer like the IBM
7094. Most of the calculation time is spent evaluating the

determinant of $(H-E)$ as a function of energy to deter-
mine the roots or eigenvalues at a given point in the
Brillouin zone. A convenient technique for evaluating
the determinant of this complex matrix has been
suggested by Soven.[17] The present calculations have
included about $(40)\times(2)=80$ basis functions, except
in the vicinity of the Fermi energy, where this number
has been increased to about 100 or 120. In calculating
the matrix elements, a total of seven terms were in-
cluded in the sum over l. At a given point in the Brillouin
zone, the calculations have been carried out on a uni-
form energy mesh, with an energy interval $\Delta E=0.02$
Ry. Slightly less than 3 min of computer time was re-
quired to set up and evaluate the determinant of an
80×80 matrix for a total of 60 energies. In order to
determine the spin-orbit splittings accurately, it was
often necessary to carry out the calculations on a finer
energy mesh.

The calculations have been carried out on a discrete
mesh within the first Brillouin zone, the mesh interval
Δk_i being given by

$$\Delta k_1 = \tfrac{1}{12}b_1; \quad \Delta k_2 = \tfrac{1}{12}b_2; \quad \Delta k_3 = \tfrac{1}{8}b_3.$$

This corresponds to 1152 points in the first Brillouin
zone and involves 95 calculations in 1/24 the zone. Of
these, six are at the symmetry points, 27 are along
symmetry lines, 41 lie in symmetry planes, and 21 are at
general points in the zone.

The calculations have been carried out using a
"muffin-tin" potential that has been provided by J. T.
Waber. This potential has been derived from self-
consistent Dirac-Hartree-Fock-Slater atomic calcula-
tions using an assumed atomic configuration of $(5d)^6(6s)^1$
for rhenium.[18] The "muffin-tin" potential has been cal-
culated by spherically averaging the superposed atomic
potentials, using the same techniques that have been
described previously in an energy-band study of the $3d$
transition series.[19]

IV. RESULTS

A. Energy Bands

The relativistic energy bands for rhenium are plotted
along the symmetry directions of the hexagonal Brillouin
zone in Figs. 2 and 3. In both figures, the zero of energy
coincides with the constant potential between the APW
spheres. The results shown in Fig. 2 include the Darwin
and mass-velocity corrections, but not spin-orbit cou-
pling. The symmetry characteristics of the various
states are identified using the single-group notation of
Herring.[12] The corresponding results for the complete
relativistic calculations are shown in Fig. 3. The latter
results have been obtained from calculations involving
unsymmetrized basis functions. As mentioned in the

[14] J. H. Wood, Phys. Rev. **126**, 517 (1962).
[15] R. J. Elliott, Phys. Rev. **96**, 280 (1954).
[16] L. M. Falicov and M. H. Cohen, Phys. Rev. **130**, 92 (1963).

[17] P. Soven, Phys. Rev. **137**, A1706 (1965).
[18] D. Liberman, J. T. Waber, and D. T. Cromer, Phys. Rev. **137**, A27 (1965).
[19] L. F. Mattheiss, Phys. Rev. **134**, A970 (1964).
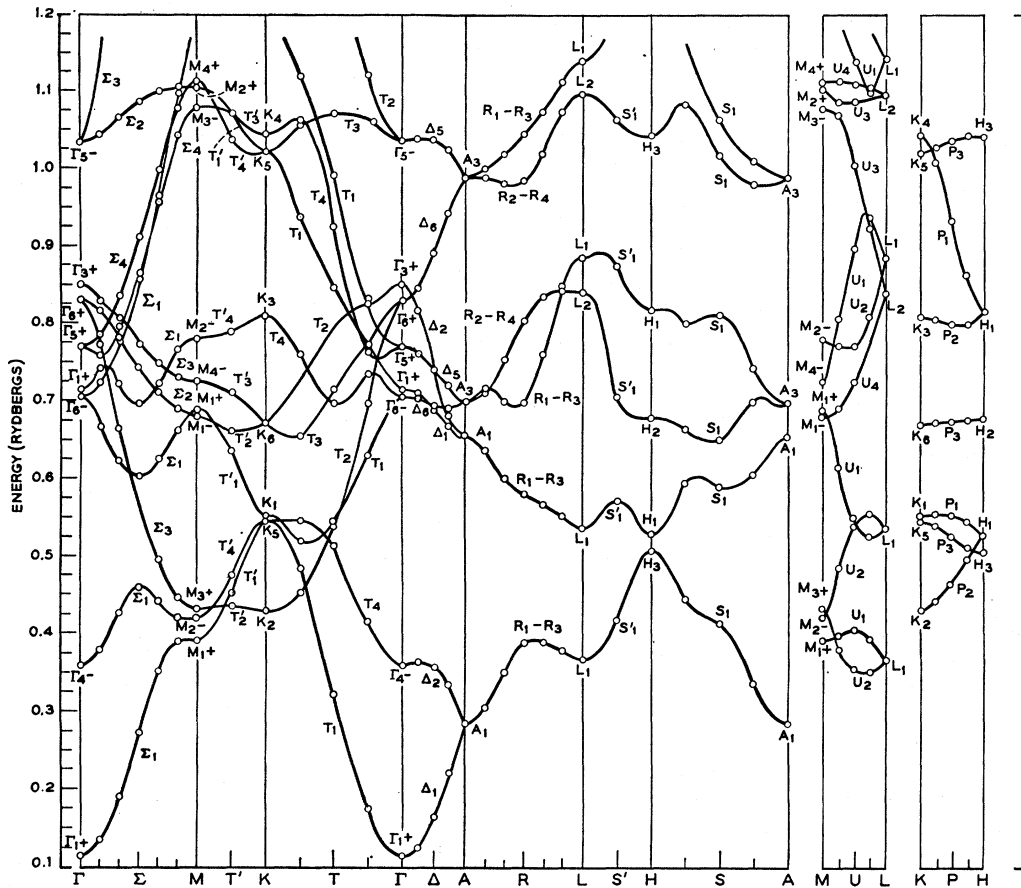
FIG. 2. The relativistic energy bands for rhenium, plotted along symmetry directions of the Brillouin zone, with spin-orbit coupling neglected.

previous section, the proper connectivity of the bands in most symmetry directions is assured by the fact that there exists only one "extra" representation for the double group. Since band crossings are possible in the Δ, P, S, and S' directions, the connectivity of the bands in these directions in Fig. 3 is somewhat uncertain. However, by performing calculations at closely spaced intervals along these directions, it has been possible to determine the proper connectivity, especially near the Fermi energy, which is indicated by the dashed horizontal line in Fig. 3.

The results shown in Figs. 2 and 3 include all of the rhenium $5d$ bands as well as the lower portions of the $6s$ and $6p$ bands. In both figures, the $5d$ bands extend roughly from 0.35 to about 1.15 Ry, yielding a $5d$ bandwidth of something like 0.80 Ry. Although the wave functions which correspond to the results of Figs. 2 and 3 have not been calculated, certain aspects of these results are clear. The lowest Γ_1^+ state in Fig. 2 represents the bottom of the $6s$ conduction band. The next state at Γ has Γ_4^- symmetry. This state presumably represents a combination of antibonding $6s$-type orbitals plus $5d$-type states. The remaining states at Γ are un-

doubtedly rather pure $5d$-type states, with the exception of Γ_3^+, which is $6p$-like.

Detailed expressions for the tight-binding wave functions which exhibit the proper symmetry characteristics for the hexagonal single-group have been tabulated by Altmann and Bradley.[20] These results are summarized in Table I, where the angular momentum content of the various representations is indicated. Since the hexagonal close-packed structure contains two atoms per unit cell, there are ten rather than the usual five d bands. This is consistent with the results of Table I. By comparing the results of Table I with those of Fig. 2, it is clear that the proper number of states having the proper symmetry exists within the energy range of the rhenium $5d$ bands.

The effects of spin-orbit coupling on the rhenium band structure are quite obvious from a comparison of the results shown in Figs. 2 and 3. Except along the AL line, spin-orbit coupling reduces all fourfold degeneracies to pairs of doubly degenerate states. The magnitude of the splittings depends on the position of the wave vector in

[20] S. L. Altmann and C. J. Bradley, Rev. Mod. Phys. 37, 33 (1965).
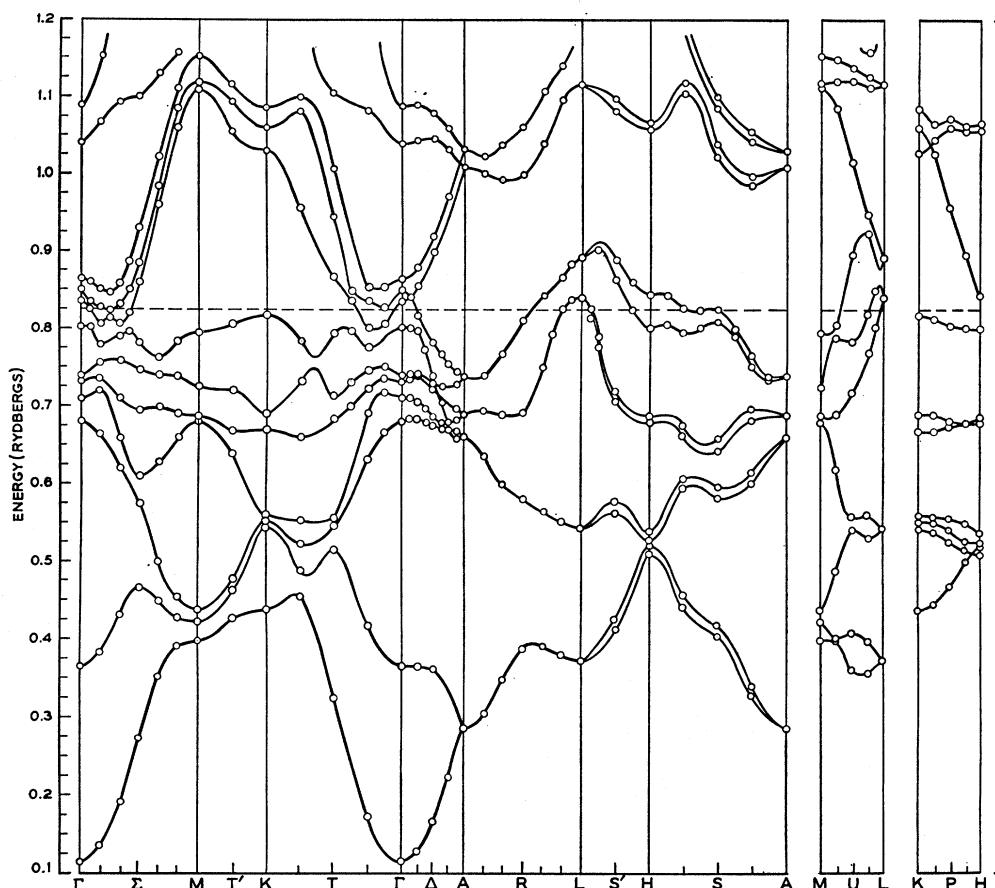
FIG. 3. The relativistic energy bands for rhenium, including the effects of spin-orbit coupling.

TABLE I. The angular-momentum content of the APW wave functions at symmetry points in the hexagonal Brillouin zone. Blank entries indicate spherical harmonics which are absent because of symmetry. The dimension of the various representations D is also given.

	D	$l=0$	$l=1$	$l=2$		D	$l=0$	$l=1$	$l=2$
Γ_1^+	1	s		d	M_1^+	1	s	p	$2d$
Γ_2^+	1				M_2^+	1			d
Γ_3^+	1		p		M_3^+	1		p	d
Γ_4^+	1				M_4^+	1		p	d
Γ_5^+	2		p	d	M_1^-	1			d
Γ_6^+	2			d	M_2^-	1	s	p	$2d$
Γ_1^-	1				M_3^-	1		p	d
Γ_2^-	1		p		M_4^-	1		p	d
Γ_3^-	1								
Γ_4^-	1	s		d	A_1	2	s	p	d
Γ_5^-	2			d	A_2	2			
Γ_6^-	2		p	d	A_3	4		p	$2d$
K_1	1		p	d	L_1	2	s	$2p$	$3d$
K_2	1			d	L_2	2		p	$2d$
K_3	1		p	d					
K_4	1			d	H_1	2		p	$2d$
K_5	2	s	p	$2d$	H_2	2		$2p$	d
K_6	2		p	d	H_3	2	s		$2d$

the Brillouin zone as well as the detailed symmetry of the states in question. Elliott has mentioned that the four-fold degeneracy along R is a consequence of time reversal.[15] It should be pointed out that although there are no splittings along R due to spin-orbit coupling, this interaction is not zero in this direction. In Fig. 3, spin-orbit coupling is responsible for uncrossing the R_1, R_3 and R_2, R_4 (time-reversal-degenerate) states near 0.840 Ry in Fig. 2.

By comparing the results of Figs. 2 and 3 at the center of the zone Γ, it is clear that spin-orbit coupling causes some important changes in the distribution of states in the vicinity of the rhenium Fermi energy. These changes can be understood qualitatively in terms of the tight-binding approximation. If it is assumed that the states with Γ_6^-, Γ_1^+, Γ_5^+, Γ_6^+, and Γ_5^- type symmetry are pure $5d$ states, then the tight-binding wave functions for these states can be determined from the work of Altmann and Bradley.[20] The Γ_3^+ state is assumed to be a $6p$-type state. The spin-orbit matrix elements between these symmetrized states are easily calculated by applying the appropriate unitary transformations to the full spin-orbit matrix for d-type states, as tabulated by Friedel
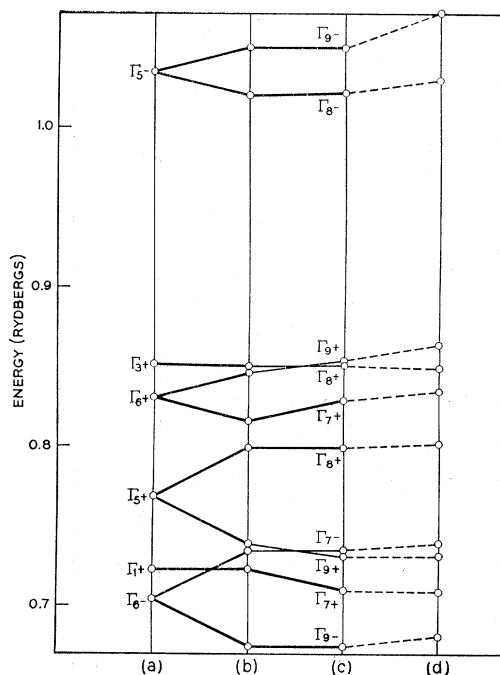
FIG. 4. The effects of spin-orbit coupling on the energy-band results at the center of the Brillouin zone. In (a), spin-orbit coupling is neglected. Using tight-binding theory, the effects of diagonal spin-orbit matrix elements are shown in (b), assuming $\xi_{5d}=0.03$ Ry. The additional effects of off-diagonal matrix elements are shown in (c). Finally, the results of the present APW calculations are shown in (d).

et al.[21] If the $5d$ spin-orbit parameter ξ_{5d} is assumed to be 0.03 Ry,[22] the results of Fig. 4 are obtained. In Fig. 4(a), the results of Fig. 2 (where spin-orbit coupling is omitted) are reproduced. In Fig. 4(b), the diagonal spin-orbit matrix elements are taken into account. Including the effects of the off-diagonal matrix elements produces additional small shifts in the energies of the various states [Fig. 4(c)]. The distribution of states that has been obtained from the fully relativistic calculation [Fig. 4(d)] is in good agreement with the results of this simplified spin-orbit calculation, as the dotted lines suggest. As we will mention later in the discussion, part of the discrepancy between Fig. 4(c) and 4(d) appears to be due to the fact that the spin-orbit parameter ξ_{5d} is energy-dependent.

The results of Fig. 2 have been obtained from symmetrized combinations of approximately 60 or 70 APW basis functions. The corresponding results of Fig. 3 have been obtained from 80 unsymmetrized basis functions (involving 40 inequivalent spatial functions). Convergence tests at various points in the zone indicate that convergence depends not only on the wave vector **k** but also on the band index n. As a result, the upper and

---

[21] J. Friedel, P. Lenglart, and G. Leman, J. Phys. Chem. Solids **25**, 781 (1964).
[22] In bcc tungsten, a spin-orbit parameter ξ_{5d} of about 0.03 Ry produces changes in the Fermi surface that are consistent with experiment. (See Refs. 1 and 2.)

lower bands in Fig. 3 are converged to within about 0.03 and 0.003 Ry, respectively. In order to obtain an accurate estimate of the Fermi surface, the results between 0.8 and 0.9 Ry in Fig. 3 have been calculated using about 100 basis functions. These results appear to be converged to within a few thousandths of a rydberg.

B. Density of States

The fully relativistic energy-band results of Fig. 3 have been extended to include a total of 95 points in 1/24 the Brillouin zone, which correspond to 1152 points in the full zone. Since the accuracy of the density of states which is calculated from this sparce sampling of the Brillouin zone is limited by poor statistics, a simple interpolation scheme has been used to calculate a more meaningful density of states. This scheme is analogous to that used in previous calculations for body-centered cubic tungsten.[1] In the hexagonal zone, it is convenient to subdivide the full Brillouin zone into small parallelepipeds, having equal sides in the basal plane $(\pi/3\sqrt{3}a)$ and a height which is about 20% smaller $(\pi/4c)$. This interpolation scheme approximates the nth band eigenvalues for a state whose wave vector lies within a given parallelepiped by a weighted average of the nth-band eigenvalues at the eight corners. The method is such that along the edges of the parallelepiped, the interpolation is linear, on the faces it is planar, and at the center the weighting factors are equal.

The results of such a calculation involving 144 000 points in the Brillouin zone are shown in Fig. 5. The histogram represents $\Delta N/\Delta E$, where ΔE is 0.005 Ry. The appropriate units for the differential density of states are shown on the left. The dotted line represents the integrated density of states, with the units shown at the right. The Fermi energy for rhenium occurs at approximately 0.825 Ry.

C. Fermi Surface

Using the fully relativistic energy-band results (Fig. 3), the intersections of the Fermi surface with the symmetry planes of the Brillouin zone have been calculated. These results are shown in Fig. 6(a). The closed hole pieces centered about the point L on the surface of the Brillouin zone have been labelled h_5, h_6, and h_7 since they correspond to holes in the fifth, sixth, and seventh zones. Similarly, those sheets labelled e_8 and e_9 correspond to electrons in the eighth and ninth zones. Since the hexagonal close-packed structure contains two atoms per unit cell, the total number of electrons and holes must be equal. An approximate calculation of the volumes of the various pieces of Fermi surface suggests that this is very nearly the case here. It is found that h_5, h_6, and h_7 correspond to about 0.0007, 0.017, and 0.15 holes/atom, respectively, while e_8 and e_9 represent about 0.16 and 0.0006 electrons per atom, respectively.
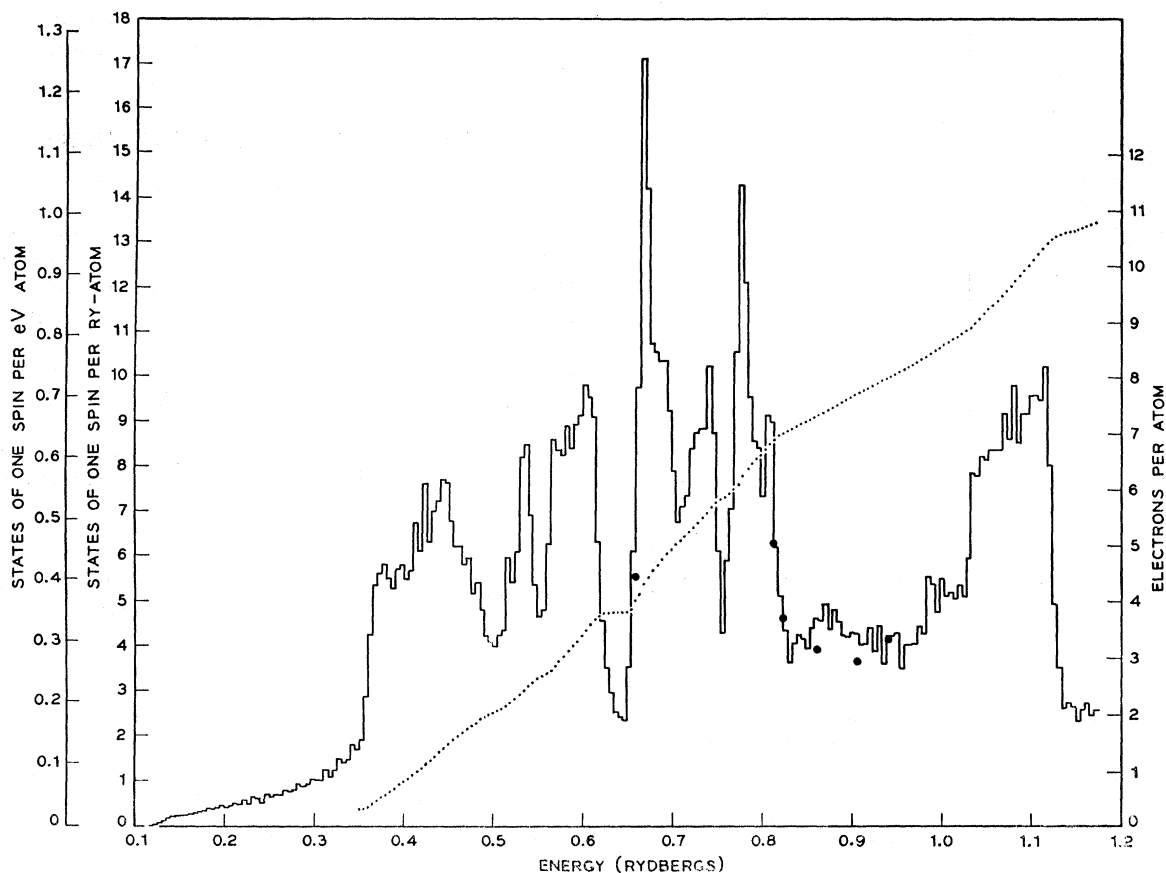
FIG. 5. Density of states for rhenium. The histogram represents the differential density of states (units to the left) while the dotted line represents $N(E)$ (units to the right). The filled circles represent experimental data, and are discussed in the text.

Several aspects of the rhenium Fermi surface are very sensitive to the exact value of the Fermi energy, which may deviate from 0.825 Ry by several thousandths of a rydberg. This is clear from Fig. 6(b), where a constant-energy surface is plotted for an energy which is 0.005 Ry higher than that assumed in Fig. 6(a). Those features of the rhenium Fermi surface which change drastically in going from Fig. 6(a) to 6(b) are considered to be less reliable than the more stable features. These less reliable features include the existence of the small closed pieces of e_8 along the AH direction.

The larger pieces of Fermi surface are sketched in Fig. 7. They consist of an open cylindrical eighth-zone electron sheet, centered about the ΓA axis and a closed seventh-zone sheet centered about the point L on the surface of the Brillouin zone. The two sheets contact along the AL line. A roughly ellipsoidal segment of this eight-zone sheet has been scooped out at the center of the zone Γ. It is clear from Fig. 3 that the rapid variation with energy of the eight-zone surface in the ALH plane is due to the flattened bands in the AH direction near the Fermi level. As a result, the ratio of the cyclotron to the free-electron mass for an orbit in this plane is estimated to be very large, on the order of 10.

The smaller segments of Fermi surface are contained within these larger seventh- and eighth-zone pieces. These include h_5, h_6, and e_9. Sketches of h_5 and h_6 are shown in Fig. 8(a) and 8(b), respectively. While h_5 appears to be nearly ellipsoidal in shape, h_6 is similar topologically to the dumbbell that Joseph and Thorsen[3] have proposed [Fig. 8(c)], though it is indented in the AL or $[10\bar{1}0]$ direction. The sheets h_5 and h_6 touch along the AL line, which is also true for the ellipsoid-dumbbell model of Fig. 8(c). The ninth-zone electron sheet tends to have the topology of a torus. However, it is uncertain whether this surface is actually multiply connected or not. [Compare Figs. 6(a) and 6(b).]

As an aid to understanding some of the more unusual aspects of the results shown in Fig. 6 and to summarize the importance of spin-orbit coupling in a rather graphic manner, the rhenium Fermi surface that is obtained by neglecting spin-orbit coupling is shown in Fig. 9. In this case, a fourfold degeneracy exists everywhere in the ALH plane so the double-zone scheme is appropriate. To simplify the comparison with Fig. 6, the single-zone scheme is used here, however. The points of contact between the various sheets of the Fermi surface are the result of accidental degeneracies at the Fermi level for
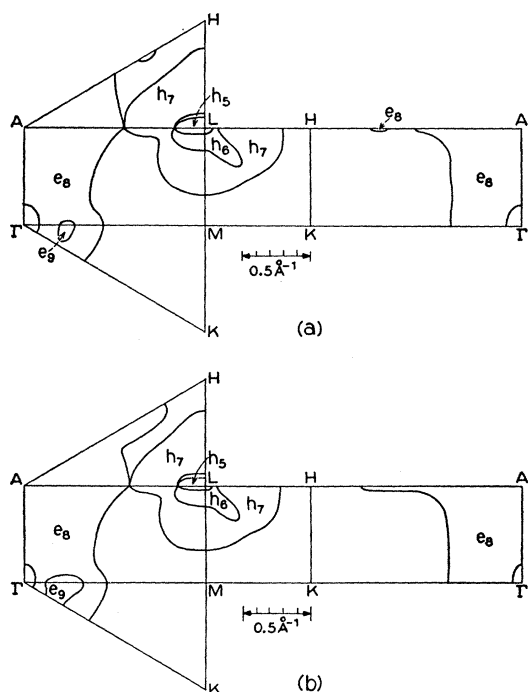
FIG. 6. Intersection of the rhenium Fermi surface with symmetry planes of the hexagonal Brillouin zone. The sheets h_5, h_6, and h_7 correspond to holes in the fifth, sixth, and seventh zones, while e_8 and e_9 represent electron sheets in the eighth and ninth zones. The results in (a) correspond to a Fermi energy of 0.825 Ry. The corresponding results in (b) indicate the changes which occur when the Fermi energy is raised 0.005 Ry.

states with even and odd symmetry in the various symmetry planes. Spin-orbit coupling introduces off-diagonal matrix elements between these states, thereby removing these degeneracies, except along the AL line. As a result of spin-orbit coupling, the connectivity of h_5, h_6, and h_7 is changed in the various symmetry planes. In addition, spin-orbit coupling pinches off the arms of e_8 which contact the zone boundary along the AH directions in the
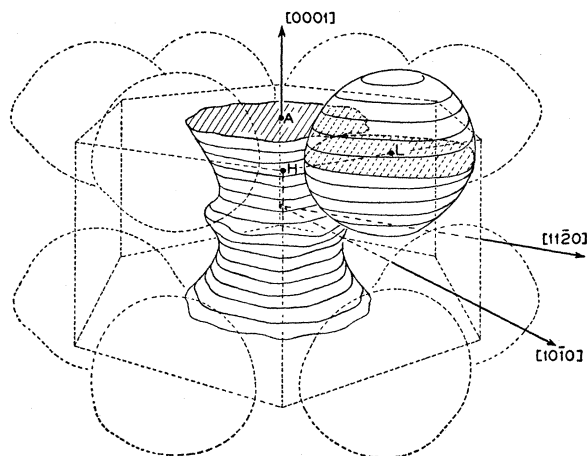
FIG. 7. Three-dimensional drawing of the seventh-zone hole and eighth-zone electron sheets for rhenium.

ALH plane. Finally, spin-orbit coupling removes the tenth-zone electron piece e_{10} and drastically alters the size and perhaps even the topology of e_9.

V. COMPARISON WITH EXPERIMENT

A. Low-Field de Haas-van Alphen Data

It is clear from Fig. 8 that the hole sheets h_5 and h_6 are similar topologically to the ellipsoids and dumbbells that Joseph and Thorsen have proposed to explain their low-field dHvA data for rhenium.[3] The main difference between the two models concerns the detailed shape of the dumbbell. According to the present calculations-the dumbbell is deformed by protrusions and indenta-

TABLE II. Extremal Fermi-surface areas for orbits which occur when the magnetic field is oriented along various symmetry directions.

H	Zone	Orbit plane	Area in $\mathrm{\AA}^{-2}$ Expt.	Theory
[0001]	h_5	(ALH)	0.0434[a]	0.046
	h_6	(ALH)	0.072[a]	0.068
	h_6	$\|(ALH)$	0.149[a]	0.157
	h_7	(ALH)		0.880
	e_8	(ALH)		1.706
	e_8	$\|(ALH)$		0.703
	e_8	(ΓMK)	0.883[b]	0.935
	e_8	(ΓMK)		0.038
[10$\bar{1}$0]	h_5	$(MKLH)$	0.00735[a]	0.007
	h_6	$(MKLH)$	0.154[a]	0.168
	h_6	rot. 60°	0.136[a]	0.152
	h_7	$(MKLH)$	0.758[b]	0.861
	h_7	rot. 60°	0.617[b]	0.663
	e_8	$(MKLH)$		0.049
[11$\bar{2}$0]	h_5	(ΓMLA)	0.025[a]	0.024
	h_6	(ΓMLA)	0.129[a]	0.136
	h_6	rot. 60°	0.147[a]	0.156
	h_7	(ΓMLA)		0.648
	h_7	rot. 60°	0.646[b]	0.697
	e_8	(ΓMLA)		0.049
	h_7-e_8	(ΓMLA)	2.86[b]	2.80

[a] See Ref. 3.   [b] See Ref. 6.

tions in the $MLKH$ plane, as shown in Fig. 8(b) [versus Fig. 8(c)].

The dimensions that are calculated for h_5 are in excellent agreement with the experimental values for the ellipsoid axes, as determined by Joseph and Thorsen. The experimental values are $a=0.219\ \mathrm{\AA}^{-1}$ along [10$\bar{1}$0], $b=0.063\ \mathrm{\AA}^{-1}$ along [1$\bar{2}$10], and $c=0.037\ \mathrm{\AA}^{-1}$ along [0001]. The corresponding theoretical values are $a=0.220\ \mathrm{\AA}^{-1}$, $b=0.066\ \mathrm{\AA}^{-1}$, and $c=0.033\ \mathrm{\AA}^{-1}$.

Table II contains a comparison between the calculated extremal areas of h_6 and the experimental results for magnetic fields along [0001], [10$\bar{1}$0], [11$\bar{2}$0]. The discrepancy between the theoretical and experimental results is generally less than about 10%. Al-

FIG. 8. Three-dimensional drawings of the fifth-zone (a) and sixth-zone (b) hole sheets that result from the present calculation. In (c), the ellipsoid and dumbbell model of Joseph and Thorsen is sketched.
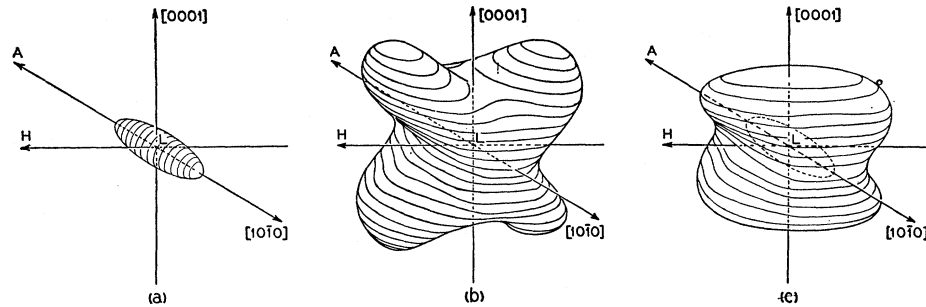
though this discrepancy is somewhat larger than that found for the ellipsoids, the general shape of h_6 appears to agree quite well with the angular dependence of the dHvA data.

The interpretation of the low-field dHvA data in terms of h_6 is analogous to that described by Joseph and Thorsen for the dumbbell. These data contain some aspects which are consistent with the modifications to the dumbbell that are suggested by the present calculations. First, as the field is rotated from [0001] towards the basal plane in either the ($1\bar{2}10$) or ($\bar{1}100$) planes, a maximum extremal area occurs between 45° and 55° from [0001]. According to the present model, this maximum occurs when the extremal orbits pass over the protrusions in the $MLHK$ plane, which are about 50° from [0001]. A rough estimate of the maximum area enclosed by such an orbit suggests a value of 0.24 Å^{-2}, which is about 25% larger than the experimental value of 0.19 Å^{-2}. This suggests that these protrusions are somewhat smaller than the calculations indicate.

Second, the dHvA data with the magnetic field in the basal plane indicate that the extremal area of the central orbit around the dumbbell decreases continuously from the $MLHK$ to the ΓALM planes. Such a continuous decrease in area is not obvious from the dumbbell model of Joseph and Thorsen without a distortion in the $MLHK$ plane, as the present calculations predict.

Third, a topology similar to that of h_6 permits a second set of noncentral extremal orbits, in addition to those which exist on the dumbbell when the field is near the [0001] direction. This second set of noncentral extremal orbits can explain the period P_5 that is observed when the magnetic field is near (or in) the basal plane. In Fig. 8(b), these noncentral extremal orbits would occur in a plane parallel to ΓALM when the magnetic field is along the LH direction. The calculated shape of h_6 suggests that this maximum extremal area coincides with the saddle point that occurs along the LH line, in which case this period presumably would not be observed.[23] However, the dHvA data indicate that this maximum extremal area occurs before the saddle point, again implying a slight modification to the shape of h_6.

[23] I. M. Lifshitz and M. I. Kaganov, Usp. Fiz. Nauk. **69**, 419 (1959) [English transl.: Soviet Phys.—Uspekhi **2**, 831 (1960)].

B. Pulsed-field de Haas-van Alphen Data

The pulsed-field dHvA data of Thorsen and Joseph[6] reproduce much of the low-field data that have been discussed in the previous section. In the present discussion, we shall confine our attention to some of the shorter periods that have been observed and discuss their interpretation in terms of the Fermi surface sections h_7 and e_8 of the present model. One of the more interesting aspects of the high-field data is the period of 3.34×10^{-9} G^{-1} which is observed when the field is along the [$11\bar{2}0$] direction. This period is readily interpreted in the present model as a closed double-zone orbit formed by e_8 and h_7 in the ΓALM plane. This corresponds to the orbit labelled β in Fig. 10. The calculated area of this orbit is 2.80 Å^{-2}, which is in excellent agreement with the experimental value of 2.86 Å^{-2}.

Most of the remaining periods that have been observed can be interpreted in terms of the seventh-zone hole piece h_7, although a few periods that are observed when the magnetic field is near [0001] seem to be associated with e_8. The calculated areas are compared with the experimental results in Table II. The shape of h_7 is similar to that suggested by the experimental data. Starting from the ΓALM plane, and rotating in 30° increments, the area enclosed by a central orbit of h_7 increases continuously from 0.648 to 0.663, 0.697, and finally to 0.861 Å^{-2}, the final value occurring in the $MLHK$ plane. The dHvA data sug-
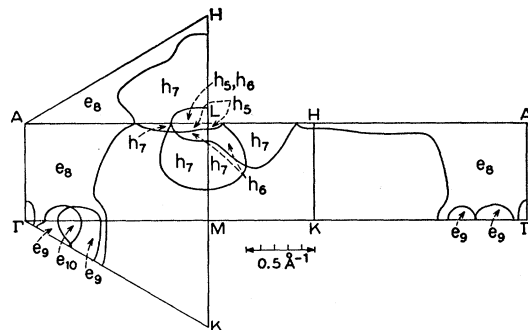
FIG. 9. Intersection of the Fermi surface for rhenium with symmetry planes of the hexagonal Brillouin zone, neglecting spin-orbit coupling.
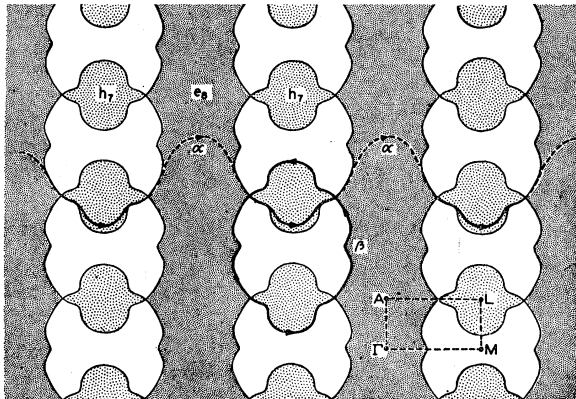
FIG. 10. Sketch of the larger sections of the rhenium Fermi surface in the ΓALM plane, showing the projection onto this plane of an open orbit α along $\langle 10\bar{1}0 \rangle$ and a closed double-zone orbit β which lies in this plane.

gest a slight decrease in area over the first 40°, followed by a more rapid increase. The calculated area associated with a central orbit in the $MLHK$ plane of 0.861 Å^{-2} is 15% larger than the experimental value. One interesting aspect of the dHvA data is the implication that the area enclosed by a central orbit on h_7 in the $MLHK$ plane is almost exactly equal to that in a plane which is rotated by 60°.

When the field is rotated in the $(10\bar{1}0)$ plane, Thorsen and Joseph observe only one period. This corresponds to the central extremal of h_7 that is rotated by 60° from ΓALM. They also observe slightly longer periods over limited angular ranges which could correspond to noncentral orbits. The corresponding orbit in the ΓALM plane is not observed. In the low-field data, smaller orbits passing through similar degeneracy points were found to be weak. In general, the form of the dHvA data in the $(10\bar{1}0)$ and $(11\bar{2}0)$ planes is qualitatively similar to that expected from the present model for h_7. In both planes, the periods associated with this piece were found to disappear when the field was within 10° or 15° from [0001]. This behavior is consistent with the shape of h_7 near the ALH plane.

C. Magnetoacoustic Data

The magnetoacoustic data of Jones and Rayne yield a limited number of extremal dimensions for some of the smaller pieces of Fermi surface in rhenium.[4] They have interpreted this data using the ellipsoid-dumbbell model of Joseph and Thornsen.[3] They have also observed oscillations which correspond to extremal dimensions which are several times larger than those expected for the ellipsoids and dumbbells. However, these oscillations were poorly defined and the corresponding dimensions were somewhat uncertain. Some of the smaller dimensions were found to be consistent with the ellipsoid-dumbbell model, others were not.

Recently, Testardi has obtained much more detailed magnetoacoustic data for rhenium.[5] In addition to the

dimensions that were found by Jones and Rayne, Testardi has observed other extremal dimensions, both large and small. The larger dimensions range roughly from 0.45 to 0.55 Å^{-1}, and agree quite well with the dimensions and shape of the seventh-zone hole surface. Most of the smaller dimensions seem to be consistent with the size and shape of the fifth- and sixth-zone hole surfaces, the ellipsoids and dumbbells of the Joseph-Thorsen model. There are some exceptions, two of which are tabulated by Jones and Rayne. These include the dimension of 0.12 Å^{-1} which is isotropic in the basal plane and a dimension of 0.08 Å^{-1} near the [0001] axis in the $(11\bar{2}0)$ plane. In the present model for the rhenium Fermi surface, these dimensions must be associated either with the small ellipsoidal pocket at Γ or the ninth-zone electron sheet e_9.

D. Magnetoresistance Data

The Fermi surface shown in Fig. 7 supports two sets of open orbits. The first set, which is directed along [0001], occurs on the cylindrical eighth-zone electron sheet e_8 whenever the magnetic field is in the (0001) plane. The second set of open orbits are along the $\langle 10\bar{1}0 \rangle$ axes and result from magnetic breakdown between e_8 and h_7. This latter set of open orbits occurs when the magnetic field is in the $(10\bar{1}0)$ plane, but not in the $[1\bar{2}10]$ direction. With the field along $[1\bar{2}10]$, the breakdown orbit closes, leaving only the [0001] open orbits.

The nature of the open orbits along $\langle 10\bar{1}0 \rangle$ is shown in Fig. 10. The open orbit labeled α results when the magnetic field is in the $(10\bar{1}0)$ plane, but not along the $[1\bar{2}10]$ axis. The dotted and solid portions of the orbit represent its projection on the $(1\bar{2}10)$ plane, the orbit passing over the rear of e_8 and the front of h_7. When the field is precisely along the $[1\bar{2}10]$ axis, these open orbits close, yielding the orbit labelled β, which has been discussed in Sec. B. The present theoretical model for rhenium also predicts the possibility of small regions of aperiodic open orbits when the field is near the $\langle 1\bar{2}10 \rangle$ axes since the open orbits along the [0001] and $\langle 10\bar{1}0 \rangle$ axes occur on the same Fermi-surface sheets.

These results are in substantial agreement with the high-field magnetoresistance data of Reed, Fawcett, and Soden.[7] They find open orbits along [0001] and $\langle 10\bar{1}0 \rangle$, the latter resulting from magnetic breakdown. They also find two-dimensional regions of aperiodic open orbits when the magnetic field is near the $\langle 11\bar{2}0 \rangle$ axes.

Reed *et al.* suggest that there are two separate sheets that are open along [0001]. This second set of open orbits along [0001] has been introduced to explain a very narrow maximum in the magnetoresistance that is observed when the current is along [0001] and the field passes precisely through the basal plane.

The present calculations predict only one surface that is open along [0001]. Since this narrow maximum represents a change in the magnitude of the magnetoresist-

ance rather than a change in its field dependence, it could result from a change in the effective mobility that coincides with the transition from extended orbits to open orbits along the axis of the cylinder e_8. According to the present Fermi-surface model, when the magnetic field is near the basal plane, there exist extended orbits along the axis of the cylinder e_8. These orbits pass through many ALH zone faces, each of which contain regions where the electron velocity is small (near S) as well as regions where interband matrix elements are expected to cause local variations in the relaxation time (near R). When the magnetic field is precisely in the basal plane and the orbits are open, a few electrons will pass through all these regions, but most will pass through none. It is reasonable to expect that the effective mobility and therefore the magnitude of the magnetoresistance might reflect such a change in the orbit characteristics.

From the low-field behavior of the magnetoresistance data, Reed et al. have estimated several properties of the rhenium Fermi surface. First of all, they predict that the [0001] open surface is nearly cylindrical in shape. Furthermore, they predict that the carriers on this cylindrical surface are electrons, in agreement with the present results. They estimate that this surface contains about 0.09 electrons per atom, a result that differs by less than a factor of 2 from the 0.16 electrons per atom that are calculated. They estimate that the ratio of the number of electrons enclosed by the cylindrical surface to the remaining electrons and holes in closed pieces is 0.71. The present calculations indicate that this ratio is very nearly equal to 1.0. Their model also predicts that the mobility of electrons on the open sheet is about 13 times smaller than that of the electrons and holes of the closed sheets. Since the sheets e_8 and h_7 have essentially the same dimensions and their model takes into account the extended orbits that are possible on the cylinder, this large difference in mobility is not yet understood.

E. Specific-Heat Data

The specific heat of rhenium has been measured by Morin and Maita,[24] who find that $\gamma = 5.9 \times 10^{-4}$ cal deg^{-2} mole^{-1}. This corresponds to a density of states at the Fermi energy of 0.52 states of one spin per eV atom. The calculated density of states is 0.37 in these same units. It is well known that the heat-capacity density of states is enhanced by electron-phonon interactions. McMillan has calculated this renormalization factor for rhenium, as well as for other transition metals and transition-metal alloys.[25] He finds a renormalization factor of 1.48 for rhenium. Using this value, the heat-capacity results of Morin and Maita imply a "band" density of states of 0.34 states of one spin per eV atom,

a value which is in excellent agreement with the present calculations.

VI. DISCUSSION OF THE RESULTS

Considering the complexity of the rhenium band structure, the agreement between the present theoretical Fermi-surface model for rhenium and the experimental data is considered to be quite good. In general, the extremal areas of this model agree with the dHvA data to within 10%. Part of this discrepancy may be due to an uncertainty in the calculated Fermi energy, even though this is estimated to be less than 0.005 Ry. It may also be due to the graphical-interpolation procedures that have been used to determine the Fermi-surface shape in the various symmetry planes. This is particularly true for the sheets h_5, h_6, and h_7 that are centered about L. The energy bands in this region are rather complicated. Many of the bands in symmetry planes, which cross when spin-orbit coupling is neglected, are uncrossed by this interaction. These effects complicate the band shapes, thereby decreasing the accuracy of the graphical-interpolation procedures that have been used to determine the Fermi surface.

In a band-structure calculation for a transition metal involving an ad hoc potential, one of the less reliable results is the relative position of the s-p bands with respect to the d bands. This parameter may be incorrect by several eV. This discrepancy is usually attributed to a lack of self-consistency in the potential or the approximate treatment of exchange effects. The size, shape, and topology of the Fermi surface often provide indirect information regarding this parameter. For example, in the case of tungsten, the dimensions of the ellipsoids at the point N are related directly to the energy difference between the Fermi energy and the $6p$-type state with $N_{1'}$ symmetry, which is a few tenths of an eV above the Fermi energy.[1]

Fortunately, a similar situation exists in rhenium. It has been found that the dimensions of h_5 and h_6 depend rather critically on the relative positions of the $6s$-$6p$ bands with respect to the $5d$ bands. This is illustrated in Fig. 11, where a limited portion of the rhenium energy bands along the AL line are shown. The results of Fig. 11(a) have been obtained from a nonrelativistic calculation involving a potential derived from atomic, self-consistent, Hartree-Fock-Slater calculations.[26] The results shown in Fig. 11(b) and 11(c) are identical to those of Figs. 2 and 3, respectively. The triangles and dashed lines in Fig. 11(c) indicate the behavior expected for fully converged results. The horizontal dashed lines represent the approximate Fermi energy in each case. Starting at L, the dimensions of h_5 and h_6 along the R direction are determined by the intersection of the first fourfold degenerate band with the Fermi level. It is clear that these dimensions in Figs.

[24] F. J. Morin and J. P. Maita, Phys. Rev. **129**, 1115 (1963).
[25] W. L. McMillan (to be published).

[26] F. Herman and S. Skillman, *Atomic Structure Calculations* (Prentice-Hall, Inc., Englewood Cliffs, New Jersey, 1963).
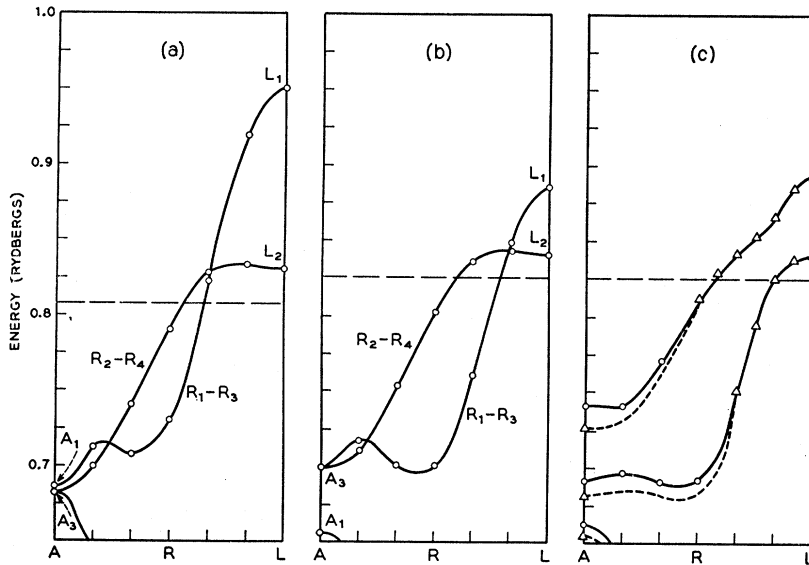
FIG. 11. A portion of the energy bands along the AL line of the Brillouin zone comparing the results of: (a) nonrelativistic calculations, (b) relativistic calculations neglecting spin-orbit coupling, and (c) relativistic calculations, including spin-orbit coupling. The dashed horizontal lines indicate the approximate Fermi levels in each case.

11(b) and 11(c) are about half the size of that shown in Fig. 11(a). According to our interpretation, the energy difference between L_1 and the Fermi level is less in Figs. 11(b) and 11(c) than in 11(a) because the Darwin and mass-velocity corrections have lowered the $6s$-$6p$ bands with respect to the $5d$ bands. The sensitivity of this L_1 state to variations in the relative energies of the s-p and d bands has also been observed in unpublished non-relativistic calculations for titanium. Since the dimension of h_5 in the AL direction agrees almost exactly with the corresponding ellipsoid dimension of Joseph and Thorsen, this implies that the $6s$-$6p$-$5d$ bands are positioned accurately with respect to one another in the present calculation.

Nevertheless, there is one feature of the present theoretical model for the rhenium Fermi surface that must be regarded as uncertain. This concerns the size, and perhaps even the existence of the ellipsoidal pocket at Γ. This section is formed by a $6p$-type state which is about 0.025 Ry above the Fermi energy. In the nonrelativistic calculation that has been described in connection with Fig. 11(a), the corresponding state was about 0.15 Ry above the estimated Fermi level. Since this piece is closed, it should easily be observed in dHvA data regardless of the magnetic-field orientation. The absence of such evidence suggests that the $6p$ state Γ_3^+ actually lies below the rhenium Fermi level.

It is interesting to examine the effects of the Darwin and mass-velocity corrections on the band structure of rhenium, since our interpretation of the results of Fig. 11 suggest that they are important. The most fundamental way of looking at these relativistic corrections is to consider their effect on the logarithmic derivatives. This is shown in Fig. 12. In Fig. 12(a), the logarithmic derivatives $(2l+1)u_{nl'}(R_n,E)/u_{nl}(R_n,E)$ are plotted as a function of energy for the rhenium $6s$, $6p$, and $5d$ bands. The relativistic equivalents to the logarithmic

derivatives [namely, $l\eta_l^-(R_n,E)+(l+1)\eta_l^+(R_n,E)$] are plotted in Fig. 12(b) (solid lines). The latter values have been used in calculating the results of Figs. 2 and 3. In both cases, the zero of energy coincides with the constant value of the "muffin-tin" potential. The main effect of the Darwin and mass-velocity corrections is to lower the energies of the $6s$-$6p$ bands with respect to the $5d$ bands. The $5d$ bands extend roughly from the energy where the $l=2$ terms become negative to the singularity in the logarithmic derivative. This singularity occurs when the function $u_{5d}(R_n,E)$ (or its relativistic equivalent) vanishes at the sphere radius.

To a good approximation, the bottom of the $6s$ conduction band is determined by the condition that

$$\eta_{l=0}^+(R_n,E)/E = (\Omega/8\pi R_s^2 - R_s/3)/8\pi R_s^2, \quad (14)$$

a result which follows from Eqs. (6) and (10) if $k_i = k_j = 0$. The energies at which Eq. (14) is satisfied are represented by $E_c(6s)$, near the bottom of Figs. 12(a) and 12(b). The difference in energy, 0.272 Ry, represents the shift in the bottom of the $6s$ band due to the Darwin and mass-velocity corrections. Herman and Skillman have obtained atomic estimates of these corrections using first-order perturbation theory and self-consistent Hartree-Fock-Slater wave functions.[26] They find a value of about 0.13 Ry, which is about half the value found above. This factor of 2 difference appears to be due to renormalization effects as well as changes in the $6s$ radial charge density that result from solving the Dirac rather than the Schrödinger radial equation. The renormalization factor is expected to be appreciable since the $6s$ nonrelativistic wave function is quite extended; the outermost maximum in the radial wave function occurs outside the APW sphere radius.

In addition to the effects of the Darwin and mass-velocity corrections on the logarithmic derivatives, it is also interesting to examine the energy dependence of the
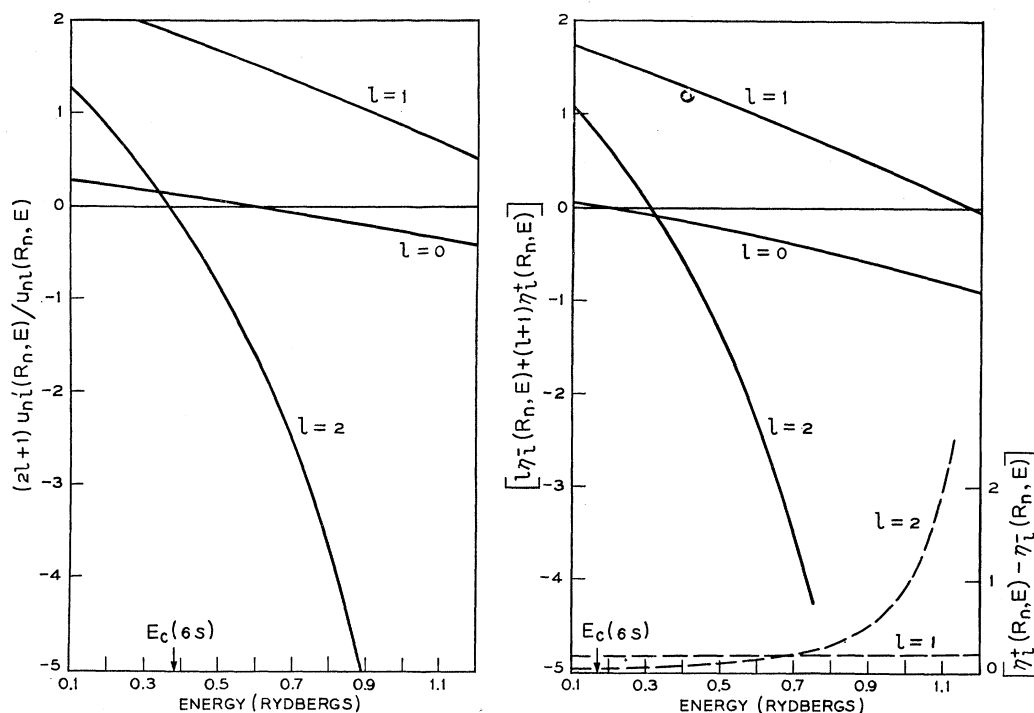
FIG. 12. Plot of the energy dependence of the logarithmic derivatives (a) and their relativistic equivalents (b) for the rhenium $6s$, $6p$, and $5d$ bands. The dashed lines in (b) (using the scale to the right) indicate the energy dependence of the spin-orbit terms in the Hamiltonian matrix for $6p$- and $5d$-type states. The arrows labelled $E_c(6s)$ indicate the bottom of the $6s$ conduction bands in the nonrelativistic and relativistic limits, respectively.

spin-orbit terms $[\eta_l{}^+(R_n,E)-\eta_l{}^-(R_n,E)]$. These terms are shown by the dotted curves in Fig. 12(b) for $l=1$ and 2. The corresponding values for higher angular momenta fall off very rapidly, the $l=3$ value being two orders of magnitude smaller than those for $l=1$. Note the sharp rise in the $l=2$ term near the top of the $5d$ band. Although the $l=1$ term is relatively flat in this energy range, it exhibits a similar behavior near the top of the $6p$ band.

Despite the fact that the spin-orbit parameter ξ_{5d} is related to $[\eta_l{}^+(R_n,E)-\eta_l{}^-(R_n,E)]$, is it not clear how one can extract an estimate of this parameter from the results of Fig. 12(b). However, an estimate for the spin-orbit parameter ξ_{5d} can be obtained by applying the tight-binding model to interpret the spin-orbit splittings that are calculated via the APW method. The results of Fig. 4 represent such an attempt for hexagonal rhenium, where ξ_{5d} is assumed to be 0.03 Ry. The calculated spin-splittings appear to be larger near the top of the $5d$ band, implying that the spin-orbit parameter is energy-dependent. The energy dependence of ξ_{5d} is evident also in the results of a relativistic band-structure calculation for tungsten by Loucks.[2] Calculations for hypothetical body-centered rhenium (using the same sphere radius and the appropriate lattice constant to assure touching spheres) plus the present hexagonal results suggest that ξ_{5d} varies from about 0.035 Ry near the middle of the $5d$ band to about 0.043 Ry near the

top of the band. This behavior seems to be consistent with the energy dependence of the $5d$ wave functions. Wood has shown (in the case of iron) that although the d radial wave functions are rather diffuse near the bottom of the d band, they become more localized than the corresponding atomic states near the top of the band.[27] This variation in the radial character of the $5d$ wave functions could easily lead to an energy-dependent spin-orbit parameter ξ_{5d}.

According to Fig. 5, the density-of-states for rhenium exhibits several peaks below the Fermi level (0.825 Ry). Above this energy, there is a broad minimum followed by maximum near the top of the $5d$ band. Assuming a rigid-band model for the hexagonal $5d$ transition metals and their alloys, it is interesting to plot the values for the band density-of-states that have been calculated by McMillan for these materials.[25] McMillan has carried through such calculations for Hf, Re, and Os, as well as the disordered hexagonal alloys $W_{0.88}Re_{0.12}$, $Re_{0.70}Os_{0.30}$, and $Re_{0.30}Os_{0.70}$. These results are shown by the filled circles in Fig. 5. The agreement between the experimental points and the theoretical curve is well within the accuracy of the calculated density-of-states. Equally good agreement has been obtained for the $5d$ body-centered cubic metals and their alloys, using a density of states that has been calculated for tungsten.[25] These

---

[27] J. H. Wood, Phys. Rev. **117**, 714 (1960).

results clearly suggest a rigid-band model, not only for transition metals, but for their alloys as well.

ACKNOWLEDGMENTS

The author has benefited from numerous discussions with several of his colleagues, including P. Soven, M. Lax, L. R. Testardi, J. H. Condon, W. A. Reed, and E.

Fawcett. The author is grateful to J. H. Wood for his aid and advice concerning the conversion of his body- and face-centered cubic nonrelativistic APW programs to the hexagonal structure. Finally, the author wishes to thank T. Loucks for providing a copy of his body-centered cubic relativistic APW program and J. T. Waber for providing the potential that has been used in the present calculation.

Selection Rules for Scattering Processes in Crystals

J. ZAK

Department of Physics, Technion—Israel Institute of Technology, Haifa, Israel

(Received 31 May 1966)

Different approaches in finding selection rules for scattering processes in crystals are discussed. It is shown that both the subgroup and the full-group procedures lead, not only to the same selection rules, but also to the same formula for finding them. The final result is expressed in terms of characters of small representations of the groups of **k**, and it is a matter of taste which procedure to use in deriving the formula for selection rules.

I. INTRODUCTION

THERE are four different results in the literature for finding selection rules for transitions between different points in a Brillouin zone. The first one is by Elliott and Loudon[1] and is based on the use of subgroups, connected with specific vectors **k**, of the full space group. Very soon afterward, another paper on selection rules was published by Lax and Hopfield.[2] The derivation in this paper was also based on a subgroup method, and their final formula contained the characters of the groups of **k** only. According to Lax and Hopfield the purpose in writing their paper was to show that the selection rules can be derived using only existing character tables, while Elliott and Loudon's procedure may require character tables other than those of the groups of **k**.

The next paper on selection rules in crystals was published by Birman.[3] He applied the conventional group-theoretical method for deriving selection rules by using the characters of the full space group. The formula derived by this method contains characters of the whole space group, and sums over the whole space group. The same full-group method was used in a paper by Zak,[4] but the final formula was reduced to a form where only the characters of the groups of **k** appear, and where the summation is on a very small number of elements.

The purpose of this paper is to show the connection between the four existing results for finding selection rules in crystals. As was pointed out, the first two are

based on subgroup techniques, while the last two use the conventional full-group method. There has been a discussion recently in the literature[5,6] about the advantages and disadvantages, and even about the correctness or incorrectness, of the subgroup and full-group approaches.

To settle this problem we have proved that both methods (subgroup and full group) lead not only to the same selection rules, but also to the same final formulas according to which the rules are found. Even more, we show that no two methods in fact exist, and that the subgroup method is just an advanced calculational stage of the full-group method. The final formula for the selection rules that is derived in this paper was already obtained before,[4] and it is shown that the formulas obtained by the other three methods[1-3] can be reduced to it. In particular, it is proved that there is no need for additional representations (other than the representations of the groups of **k**) in the first method,[1,7] and as a consequence of this the formula derived in the note[4] becomes identical with the results in the paper by Elliott and Loudon.[1] In Sec. II a description of the different approaches to selection rules is given. In Sec. III it is shown that all of them lead to the same formula.

II. DIFFERENT APPROACHES TO SELECTION RULES

In various transition processes in crystals an excitation (electron, phonon, exciton, etc.) is scattered from

---

[1] R. J. Elliott and R. Loudon, J. Phys. Chem. Solids **15**, 146 (1960).
[2] M. Lax and J. J. Hopfield, Phys. Rev. **124**, 115 (1961).
[3] J. L. Birman, Phys. Rev. **127**, 1093 (1962).
[4] J. Zak, J. Math. Phys. **3**, 1278 (1962).

[5] Melvin Lax, Phys. Rev. **138**, A793 (1965).
[6] J. L. Birman (private communication).
[7] Dr. Elliott has kindly approved this point in a private communication.